Mesoscopic Fabric Sheet Racks and Blocks as Catalysts with Efficiently Exposed Surfaces for Alcohol Electrooxidation

Md A. Shenashen,[1] Diab Hassen,[1] Sherif A. El-Safty, [1,2*] Naeem Akhtar,[1,2] Abhijit Chatterjee,[3] Ahmed Elmarakbi[4]

[1]National Institute for Materials Science (NIMS), Research Center for Strategic Materials,1-2-1 Sengen, Tsukuba-shi, Ibaraki-ken 305-0047, Japan.

[2]Graduate School of Advanced Science and Engineering, Waseda University, 3-4-1 Okubo, Shinjuku-Ku, Tokyo,169-8555, Japan

[3]Dassault System Biovia K.K., Materials Science Enterprise, ThinkPark Tower, 2-1-1 Osaki, Shinagawa-ku, Tokyo, 141-6020, Japan.

[4]Department of Computing, Engineering and Technology, University of Sunderland, Edinburgh Building, Chester Road, Sunderland, SR1 3SD, United Kingdom.

TeL: +81-29-859-2135

FAX: +81-29-859-2501

E-mail: sherif.elsafty@nims.go.jp; sherif@aoni.waseda.jp

http://www.nims.go.jp/waseda/en/labo.html

http://www.nano.waseda.ac.jp/

Abstract

Electrode designs based on sheet racks and blocks with multi-diffuse groove spaces and enriched active sites and scales would promote the commercial applications of electroactive materials. We report a facile one-pot hydrothermal approach to synthesize mesoscopic porous Co_3O_4 or hybrid graphene (GO)/Co_3O_4 sheet-on-sheet racks and blocks. Three basic types of sheet scalability racks can be built in vertical and non-stacked edge orientations, such as neat micro/nano-groove rooms, butterfly wing scales, and wall groves, leading to highly exposed surface converges and sites. In particular, the stacked S-GO/Co_3O_4 sheet-on-sheet blocks can be oriented in vertical tower buildings. The atomic structures of the developed Co_3O_4 catalysts were dominant along the highly dense {112/111} interfaces and single crystal {111} and {112} facets. The electrochemical performance of the mesoscopic porous Co_3O_4 catalyst toward alcohol electrooxidation was evaluated in alkaline conditions. The mesoscopic hybrid GO/Co_3O_4 racks revealed superior catalytic activity in terms of oxidation currents and onset potentials, indicating the effect of the synergetic role of active Co^{3+} sites along the densely exposed {112} facets, graphene counterparts, and hierarchically non-stacked sheet racks on the electroactive functionality. Results indicate that the mesoscopic GO/Co_3O_4 sheet catalyst is suitable for highly efficient electrochemical reactions.

1. Introduction

The increasing demands for environmentally-friendly energy resources have triggered ideas for developing high-performance energy resources with low cost and zero emission. [1–4] Fuel cells have received considerable attention as promising candidate to satisfy the increasing global energy demand. [5] Recently, intensive investigations have focused on alcohol fuel cells (i.e., direct methanol and ethanol fuel cells) as alternative energy-generating devices owing to their high power density, low maintenance cost, simplicity, and low operating temperature. [6,7] However, the applicability of direct alcohol fuel cells (DAFCs) is hindered by electrode materials. Advanced low-cost materials with high catalytic activity have been explored to improve the overall performance of alcohol fuel cells. [8] In particular, the development of highly efficient and low-cost electrode materials with morphologically- and anisotropically-controlled growth, as well as multi-diffusion-controlled voids, remains a great challenge for the practical applications of the alcohol fuel cells. [9,10] The features of catalytic surfaces are significant in the electrooxidation of organic molecules. [11] Catalysts with tailored building, controlled surface morphologies, and uniform mesopores provide abundant electroactive

surfaces for preferential adsorption of reactants, fast electron transport at electrode/electrolyte interfaces, and enhanced kinetics of molecule electrooxidation reaction. [12,13]

Transition metal oxides and their composites are attractive electrocatalysts for the direct oxidation of alcohols because of their high electrocatalytic activity and low cost. [14] The electroactivity of the transition metal oxides is mainly dependent on the surface functionality of the catalytic materials. [15,16] Furthermore, the smartly integrated and multi-component nanoarchitectures might offer synergetic properties and outstanding advantages than those of individual components, such as the largely enhanced electronic configuration, superior structural stability and flexibility, ultra-fast electron transfer efficiency, and more electroactive sites. [17–20] Among them, Co_3O_4 has received considerable attention because of its intriguing advantages, such as excellent capacitive, tunable textural features, improved thermodynamic stability, and easy preparation at low cost.[17–19] In addition, Co_3O_4 mesocrystals have shown high catalytic activity associated with good electrical conductivity and easy charge transport. [20] However, their poor recyclability and long term stability still hinder their practical application. [21] Interestingly, the electrochemical activity of Co_3O_4 can be efficiently improved by enhancing the surface architecture with highly active sites and exposed facets. [20]

Nanohybrid-based catalysts integrate the unique features and characteristics of the components, and usually they show synergistic enhancement in electroactivity as a result of the cooperative contribution of constituents.[21] Modification of Co_3O_4 with highly conductive carbonaceous materials such as carbon nanotubes, carbon black, and graphene is a potential way to improve the electrochemical performance of Co_3O_4. [17,21] Specifically, graphene was validated as a good catalyst support because of its unique characteristics of high electrical conductivity, high specific surface area, good chemical stability, and good corrosion resistance. [22–24]

A straightforward, one-step synthesis of GO/Co_3O_4 sheet racks and S-GO/Co_3O_4 sheet-on-sheet blocks was developed in this study. Control over the anisotropic morphological and sheet scalability in different orientational racks of (i) neat micro/nano-groove rooms, (ii) butterfly wing scales, and (iii) wall groves leads to efficiently exposed surface catalysts for DAFCs. The fabrication route provides stacked S-GO/Co_3O_4 sheet-on-sheet blocks that can be oriented in a vertical tower building. The vertically developed sheets with multi-functional mesoscopic voids and hocks, active surface components, and high index crystal planes boost the electrocatalytic activity (Scheme 1). Significantly, the sheet racks with mesospace-window hooks, dense and active {112}/{111} Co^{3+} and O^{2-} sites, long-range sheet ordering,

vertical sheet racks, mimicked sharp-pointed outgrowth prickles covering sheath surfaces, and non-stacked layers enable electron diffusion and movements with little resistance and ensure contact between every mesocrystal surfaces and electrolyte with a multi-directional accessibility. Our findings showed that the GO/Co_3O_4 electrode revealed outstanding catalytic activity for ethanol and methanol electrooxidation compared with S-GO/Co_3O_4 blocks and pristine Co_3O_4 catalyst. More specifically, the low onset potentials and high oxidation current of the GO/Co_3O_4 indicate the significant role of the integrated GO, high-index crystal facets, and hierarchal sheets oriented in grooves, groves, and butterfly wing scales. The GO/Co_3O_4 sheet racks exhibit enhanced long-term workability of up to 10000 s, demonstrating better structural stability and may serve as efficient and cost-effective electrocatalysts for alcohol oxidation.

(Scheme 1)

2. Results and discussion

2.1. Vertical growth mechanism of mesoscopic sheet-on-sheet racks and blocks

Structural directing agent (SDA) templates, such as hexamethylenetetramine (HMTA) or urea, were used to control the vertical growth alignment of Co-based nanostructures in rack- or block-shaped buildings under hydrothermal conditions. Considering the simplicity of our synthesis strategy (**Table S1, Figures S1–S3**) and the initial reaction precursors ($CoCl_2$, HMTA, and urea) of the as-obtained products, the chemical structure composition of the corresponding rack- or block-shaped nanostructures could have obviously formed through a number of consecutive reactions. Briefly, the hydrolysis of urea/HMT generated OH^-, which subsequently reacted with Co^{2+} species to form hierarchical cobalt carbonate hydroxide [$Co(OH)_x(CO_3)_{0.5}\cdot 0.11H_2O$] **(Figure S3)**. The addition of SDA to the reaction solution led to the formation of a soluble complex and facilitated the recrystallization of $Co(OH)_x(CO_3)_{0.5}\cdot 0.11H_2O$ nanocrystals. Furthermore, the negatively charged oxygen functional groups of the GO sheet offered reliable mediators for the growth of nanocrystals through the electrostatic interaction between the positively charged Co^{2+} species and the functional surface groups. More importantly, the hierarchically morphological control of GO/Co_3O_4 was dependent on the addition of urea or HMTA agents to used cobalt salt. This finding suggested that HMTA and urea play a key role in the formation of non-stacked or stacked sheet-on-sheet architectures with rack- and block-like structures. The orientational building architecture mechanism possibly controlled the vertical growth alignment of stacked S-GO/Co_3O_4 sheet-on-sheet blocks and non-stacked sheet racks with different shapes, such as neat micro- or nano-groove rooms, butterfly wing scales, and wall groves.

Particularly important is that the addition of urea allowed for the fast anisotropic growth of crystals, leading to the formation of thermodynamically stable nuclei sites. Soon after the sheet-like structure was formed, the urea adsorbed on the surface of these sheets facilitated their attachment to the neighboring molecules. To this end, the subsequent sheet-by-sheet stacking of the block structures gave rise to a much larger tower-like building with exposed smooth and flat surfaces (**Figures S1G and S1H**). In turn, the introduction of HMTA into the solution system was crucial for the formation of rack-like structures. Specifically, urea species allowed for the slow crystal growth of the precursor in vertical direction and formed complexes with Co^{2+} in the solution, thereby leading to the retarded movement of cations. Consequently, the formation of $Co(OH)_x(CO_3)_{0.5}{\cdot}0.11H_2O$ was delayed. As a result, this interaction favored the intergrowth that led to the hierarchical 3D-like racks with a wide range of morphologies, such as neat micro- or nano-groove rooms, butterfly wing scales, and wall groves (**Figures S1A–S1F**).

Under further thermal treatment at ~400 °C, the coordinated H-bonding of cobalt carbonate was preferably rearranged to generate Co_3O_4 or GO/Co_3O_4 sheet racks in three different basic shapes, namely, (i) neat micro/nano-groove rooms, (ii) butterfly wing scales, and (iii) wall groves; however, the stacked S-GO/Co_3O_4 sheet-on-sheet blocks can be oriented in vertical tower buildings (**Figure 1**). Significantly, the hierarchal orientations in sheet racks or sheet-on-sheet blocks play key roles in the crystal growth, dominating facets along highly dense {111/112} interfaces and single crystal {112} or {111} facets, respectively (**Figures 1 and 2**).

(Figure 1 and Figure 2)

2.2. Hierarchy levels of GO/Co_3O_4 racks and S-GO/Co_3O_4 blocks

The field-emission scanning electron microscopy (FE-SEM) micrographs (**Figures 1(A–D) and S1**) and 3D molecular structure simulation (Figure 1E–1H) of GO/Co_3O_4 racks and S-GO/Co_3O_4 blocks were utilized. For the first time, FE-SEM micrographs provided a clear evidence of well-controlled morphology and molecular orientations of sheet racks, neat micro/nano-groove rooms (A), butterfly wing scales (B), and wall groves (C). Figure 1A shows massive sheets connecting and overlapping in neat micro/nano-groove rooms like the tiles on an electrode surface archery. In addition, a group of sheet branches and scales growing in densely tangled thickets form butterfly wing scales (Figure 1B). The flat and broad sheets are tacked with a pale tip at the end of each flat branch. The tip is connected in a center point, creating angle with open degree space. In another top-view, the micrograph shows the

formation of vertically aligned, non-stacked surface-structured wall groves and non-stacked and fabric ordering layer-on-layer sheet design patterns **(Figure 1C).** All orientational shapes showed key features of dense particle-unit-blocks and smart non-stacked layer architecture with uniform micro-, meso-, and globule pores. In turn, FE-SEM image (Figure 1D) shows the stacked sheet blocks oriented in a vertical tower building. Note that the addition of GO has no effect on the structural stability and integration of sheet racks and blocks with uniformly spaced layers, which are probably responsible for the efficient electro-activity with high diffusivity of electrons during the reaction.

The absence of extended GO network sheets in the SEM investigation was possibly due to the small amount of GO embedded in the GO/Co_3O_4 hybrid sheets. Moreover, during the *in situ* Co_3O_4 crystal growth, the electrostatic GO-to-Co^{2+} binding interactions occurred. Thus, part of the GO loaded was possibly consumed during the vertical directional growth of Co_3O_4 nanocrystals. After a prolonged period of crystal growth, the GO sheets were fully wrapped by Co_3O_4 nanocrystals because of the integrative stacking of the generated sheet-on-sheet layers or sandwich-like architectures. Furthermore, the high angular annular dark-field scanning transmission electron microscopy (HAADF-STEM) images (**Figure S2**) showed further evidence of the formation of sandwich-like layer structures (**Figure S2A**). In addition, the micrographs showed that the GO sheets were embedded in the hierarchical sandwich building at the edges (**Figure S2A**) and in the inner cores of both the hierarchically stacked S-GO/Co_3O_4 sheet-on-sheet blocks and GO/Co_3O_4 non-stacked sheet rack-like wall groves (**Figure S2B**). [25]

The nanoscale molecular arrangement of structures shows clear evidence of the mimicked formation of these three orientational sheet racks (E–G) and rigid blocks in a vertical tower (H). For example, **Figure 1E** shows that the groove room scales vary considerably in shape, some being rectangular, whereas others are triangular tiles or plumes. The HAADF-STEM pattern (I, center) shows that the triangular tile formed between sheet boulders over the domains created markedly dense branches growing in clumps, which is a characteristic of the multi-diffused rooms for alcohol molecules. This prismatic edge scale of the sheet racks (**Figure 1I**) might typically measure about 90–100 nm thickness, although the sheet platelet is 1.5–2.0 μm in width, leading to highly exposed surface converges.

A closer look into the HAADF-STEM image (**Figure 1J**) of the top surface of sheet racks reveals the surface construction with encrusted branches of sharp and pointed outgrowth of prickle-like prismatic ridges. As a result of passing through marginally prismatic ridges on the surface of the sheet scale, almost all alcohols that hit active site surfaces can be absorbed and

captured to generate more energy. The outer surface of the "blade edge" covered with protruding nanoscale ridge-like arms is hooked to the ethanol/methanol molecules. The flat-plate is fully covered with bumps or drop-like Co_3O_4 MC scales. The density of bumps or drop-like Co_3O_4 MCs is considerably organized and homogenous, giving the sheets a wide-range domain of exposed, dense, and active Co^{3+} and O^{2-} sites along the {111} and {112} surfaces (**Figure 2A–2F**). The high-magnification HAADF-STEM image of nanosized particle indicates that the Co_3O_4 mesocrystals (MCs) are grown along {111} and {112} dominant facets (Figure 1H). The electron diffraction (ED)-STEM image (Figure 1K) shows the abundant resolutions of low- and high-index lattice planes of (−1−11) or (−4−44), (33−3), (−26−2), and (−531) fringes around the {112}-principle zone-dominant plane. The preferential orientation of Co_3O_4 crystals with high-index {112} facet and {111/112} interfaces (Figure 1J and 1K), as well as highly active Co^{3+} exposure (Figure 2E and 2F) with sophisticated morphology, are expected to play a crucial role in the catalytic performance of Co_3O_4 MCs. The HAADF-STEM image of S-GO/Co_3O_4 rigid sheet-on-sheet blocks shows atomic plane distances of 1.65 and 2.859 Å of the high- and low-index facets of (4−2−2) and (−220) or (02−2) lattice planes around the {111}-principle zone dominant plane (**Figure 2C and 2D**).

The crystal structure and composition of mesoporous Co_3O_4 and hybrid sheet GO/Co_3O_4 racks or S-GO/Co_3O_4 blocks was identified by wide angle X-ray diffraction (**Figure S4**) and Raman spectra (Figure 3A). All the observed diffraction peaks of mesoporous Co_3O_4 can be perfectly assigned to standard face-centered-cubic (*fcc*) (space group: *Fd3m*, JCPDS 42-1467) Co_3O_4. [26,27] No impurity peaks were detected, indicating the formation of pure Co_3O_4 phase. Furthermore, the weak diffraction peak at 25° is due to the (200) diffraction of GO. [28] Our findings proved that GO has been successfully reduced through the hydrothermal treatment. Moreover, the reduction of GO facilitated the formation of Co_3O_4 as a result of the strong electrostatic interactions between the oxygen surface groups of GO and Co_3O_4 MCs. As seen in **Figure 3A**, the Raman shift spectra of the samples clearly exhibit well-defined peaks centered at 478.9, 521.7, 621.4, and 685.6 cm^{-1} corresponding to the vibrational modes of Eg, F_{2g}^{1}, F_{2g}^{2}, and A_{1g} of Co_3O_4. [29] The highly intense peaks located at 1350 and 1605 cm^{-1} are caused by the E_{2g} vibrational mode of the second-order band (sp^2) of the graphitic carbon, [30] as evidenced by the X-ray photoelectron spectroscopy analysis (**Figure S5**). [31–33]

The N_2 isotherms (**Figure 3B**) showed hysteresis loops (IV-type) of mesoporous Co_3O_4 and hybrid sheets of GO/Co_3O_4 racks or S-GO/Co_3O_4 blocks. The specific surface areas of the GO/Co_3O_4, S-GO/Co_3O_4, and Co_3O_4 were measured to be 79, 58, and 42.5 m^2/g, respectively.

The enhanced surface area of GO/Co_3O_4 can be attributed to the (i) anisotropic sheet-on-sheet building with a high degree of surface uniformity demonstrating low defects; (ii) the homogeneous dispersion of metallic sheets on the surfaces of GO, which avoids the agglomeration of GO sheets and keeps their high surface area; and (iii) the creation of mesoscale voids and spaces in the interior structures. The controlled uniformity of mesopore across the hierarchical sheet racks and blocks (Figure 3B, insert) might create a potential accessibility of alcohol molecules into the catalyst matrices. Significantly, the hybrid sheet GO/Co_3O_4 racks or S-GO/Co_3O_4 blocks with multi-functional cavity pores enables the multi-accessible windows of reactant molecules to bind with interior active Co^{3+} sites during the electrochemical reaction.

(**Figure 3**)

3. Electrocatalytic activity of sheet racks towards alcohol oxidation reaction (AOR)

Several key factors significantly influence the electrochemical performances of the catalytic sheet Co_3O_4 racks and block-modified glassy carbon (**GC, see supporting information**) electrodes for AOR, including scan rate (**Figures 4A and S6**) and alcohol concentration (**Figure S7**). The effect of scan rate on the performance of the GO/Co_3O_4/GC electrode catalyst for direct oxidation of methanol was investigated over the range of 10–600 mV s^{-1} in 1 M methanol, as shown in **Figure 4A**. Results show that the anodic current was enhanced with increasing scan rate, demonstrating a diffusion-controlled process. A weak peak was observed in the reverse scan with increasing scan rate of above 100 mVs^{-1} which indicating an abundance of high valence cobalt species to be consumed in the cathodic scan to generate the related cathodic peak. [34–36] **Figure S7** shows that an increase in the anodic current was observed with increasing concentration of methanol, indicating that the oxidation of methanol at the GO/Co_3O_4/GC electrode is a rate-determining process. The relationship between the square root of the scan rate and the current density was studied to examine the methanol oxidation reaction (MOR) kinetics of GO/Co_3O_4 rack catalysts, as illustrated in **Figure S8**. The plot shows that the current density of MOR increased linearly with increasing applied scan rate, thereby confirming a controlled diffusion reaction.

(Figure 4)

The electrocatalytic performances of Co_3O_4/GC, GO/Co_3O_4/GC, and S-GO/Co_3O_4/GC electrode catalysts were initially investigated by cyclic voltammetry (CV) technique in 0.5 M NaOH N_2-saturated solution at a scan rate of 50 mV s^{-1} at room temperature (**Figure 4B–4D**). Basically, the catalytic activities of GC and GO-modified-GC electrodes for AOR are very

poor, as evidenced by CV profiles (**Figure S9**). Interestingly, the Co_3O_4/GC, GO/Co_3O_4/GC, and S-GO/Co_3O_4/GC electrode catalysts display prominent pairs of redox peaks through the anodic and cathodic sweeps as a result of the reversible reactions of Co_3O_4/CoOOH (I/IV) and CoOOH/CoO_2 (III/II) (**Figure 4B**), in agreement with the reported results elsewhere.[37] The CoOOH active components may act as mediator electroactive species on outer-surface layers to bind the adsorbed alcohol molecules, to offer more active sites, and to facilitate electron transfer during AOR (**Schemes 1**).

Clearly, the hybrid GO/Co_3O_4 or S-GO/Co_3O_4 shows broader redox peaks with a larger enclosed area than that of bare Co_3O_4, indicating higher electrochemical performances of the hybrid GO/Co_3O_4 or S-GO/Co_3O_4 catalysts. As shown in **Figure 4B** the increase in the current density follows the order GO/Co_3O_4/GC > S-GO/Co_3O_4/GC > Co_3O_4/GC, indicating the effect of the synergetic coupling between Co_3O_4 and GO with retention of the morphological sheet-on-sheet racks or blocks. Furthermore, Figure S6 shows a remarkable electrocatalytic activity of Co_3O_4-modified GC electrodes compared with Co_3O_4-free electrodes. This significant finding resulted from the morphological structure of Co_3O_4 sheet-on-sheet racks, which enhanced the electron and molecular diffusivity along the nano-scale architectures. Moreover, the actively exposed surface {112} facets and {112}/{111} interface planes with Co^{3+} and O^{2-} sites led to low surface energy and high electron density on the exposed sites (**Figure 5A**).

Figure 5 shows evidence of the actively top-surface sites of sheet racks and blocks along highly dense {112}/{111} interfaces and single crystal {112} and {111} facets that affected the AOR performances. The Co_3O_4 sheet racks with {112}/{111} interface planes showed a high degree of exposure to the top Co^{3+}-surface sites, electron density, and binding energy along the interior atomic-scale surface crystal oriented within the single {112} or {111} planes (**Figure 5B–5D**). In addition, the surface electron density map and the distribution of electrostatic potential along the {112} and {111} facets show evidence of dense electron distribution, accessible surface binding, and continuous electron movement onto the {112} top-surface compared with that of the {111} facet (**Figure 5E and 5F**). **Figure 5D–5F** shows the confined plane-to-plane stacking of alcohol-to-Co^{3+} {111}- or {112}-top-surface site binding in the axial scales, as well as the stable molecular orientation and spatial distributions of alcohol molecules onto surfaces that efficiently affected electrocatalytic AOR performance. This vertically geometric alcohol-to-surface orientation is generated around the dense electron surfaces of accessible Co^{3+} and O^{2-} sites, leading to high adsorption energy (E_{ads}) and thermodynamically stable binding energy (E_{TSB}) (**Figure 5D–5F, inserts**). The increase of

enriched Co^{3+} site surface onto the main topographic facets follow the order {111} < {112} < {112}/{111} planes, which agrees with the E_{ads} and E_{TSB} values. This finding indicates that the GO/Co_3O_4 sheet racks with {112}/{111} surface plane have highly catalytic Co^{3+} sites, which leads to efficient AOR activities.

Significantly, the DFT calculations of hybrid GO/Co_3O_4 sheet racks show the retention of the densely electrostatic potential map and surface electron distribution along the active {112}/{111}-Co^{3+} and -O^{2-} vacancy sites within 1000 cycles (data not shown). This indicates the stability of charge or electron transfer process during alcohol-to-surface interaction. The sheet rack designs with (i) neat micro/nano-groove rooms, (ii) butterfly wing scales, and (iii) wall groves may maintain the alcohol molecular dimensionality or directionality, as well as E_{TSB} with the formation of alcohol-to-surface binding into the surface of sheet racks. This enables an extensive range of AOR cycling.

Figure 5

Furthermore, the optimized theoretical studies (Scheme 1 and Figure S10) on crystal structure and electronic configurations of GO layers indicated the formation of dense electron clouds on both the top- or side-view orientations of GO (Figure S13). The electronic configuration along the GO crystal structure possibly acted as actively centered electron triggers because of the highly exposed Co_3O_4 nanocrystal facets (**Scheme 1**). The creation of strong electro-static potential onto and along the GO layer surfaces possibly generated a dense electronic configuration around the active positively (Co^{3+}) and negatively (O^{2-}) charged atoms on the top-exposed surfaces of crystal {112}/{111} interfaces. These hierarchical GO/Co_3O_4 sheet networks can significantly enhance the electrochemical reaction activity and kinetic electron diffusion (Scheme 1) along the surface layers or crystal centers of the active facets.

In case of alcoholic assay, the adsorption and dissociation of ethanol/methanol molecules take place mainly on the top-Co^{3+} active site surfaces. **Figure 4C–D** shows that the GO/Co_3O_4/GC, S-GO/Co_3O_4/GC, and Co_3O_4/GC electrodes revealed no anodic peaks during AOR, which might be attributed to the overlapping of oxygen evolution and alcohol oxidation currents. Interestingly, the absence of any peak in the reverse scan indicates that all alcohol molecules were successfully oxidized during the forward scan. This demonstrates the efficient removal of carbonaceous species and intermediates in the forward scan. Moreover, the formation of OH_{ad} species at relatively lower potentials can effectively transform the chemisorbed species and carbonaceous intermediates absorbed at the GO/Co_3O_4 surfaces into CO_2 species that evolved, leading to the release of catalytically active sites available for further

electrochemical reactions. [38] Specifically, in the DAFC assays, the electrooxidation of alcohols in the alkaline solutions led to the generation of reactive intermediates, which subsequently formed anions (Figures S11–S13). For ethanol electrooxidation, complex species were formed during the reactions. The acetaldehyde (CH_3CHO) and acetic acid (CH_3COOH) were the principal products formed at the beginning of the ethanol oxidation. In addition to these products, methane (CH_4) and ethane (C_2H_6), as well as CO adsorbate, were generated as secondary products. The intermediate (CO species) was the main poisoning product that blocked the active sites of the GO/Co_3O_4 catalyst and subsequently passivated its surface. In turn, formaldehyde (HCHO) and formic acid (HCOOH) were the main intermediates in methanol oxidation, as evidenced from the mass spectrometric (MS) analyses (Figures S10 and S12a). The HCHO solutions were possibly oxidized at the heterogeneous catalyst surfaces of GO/Co_3O_4, thereby leading to the formation of CO_2 and other intermediates, such as formate (HCO_2^-) anions. Our findings indicated the complete oxidation of HCHO to CO_2 (i.e., as a secondary product) through the decomposition of carbonate species, which is consistent with the non-active mechanism reported by Motheo et al. [39]

Figure 4C–D shows that the GO/Co_3O_4/GC electrode patterns have higher oxidation current and lower onset potential than the Co_3O_4/GC electrode in pure alkaline conditions. For example, the onset potentials of the porous GO/Co_3O_4-based electrodes are about 0.385 and 0.36 V (*vs.* Hg/HgO) for methanol and ethanol oxidation, respectively. However, the bare Co_3O_4 modified electrode displays onset potentials of 0.45 and 0.42 V (*vs.* Hg/HgO) for methanol and ethanol oxidation, respectively (Figure 4C and 4D). Interestingly, the observed onset potential for the proposed GO/Co_3O_4/GC catalyst is much lower than those of electrodes fabricated using Co_3O_4, [15,40] NiO [41], and Co_3O_4/NiO nano-crystal arrays. [40] The superior electroactivity for alcohols electrooxidation in terms of lower onset potential and remarkable current density of porous GO/Co_3O_4 racks compared with stacked S-GO/Co_3O_4 blocks indicates the effective role of dense Co^{3+} sites along densely exposed {112} or {112}/{111} facets and hierarchically non-stacked sheet racks in AOR performance.

Our findings (Figures 4C and 4D) provided evidence that the catalytic activity of the GO/Co_3O_4 rack and block catalysts toward MOR was higher than that of EOR. The AOR trend and rate are significantly correlated with the structures of alcohol (CH_3OH or CH_3CH_2OH) functional groups. The high current density with MOR (Figure 4C) indicated that the MOR kinetic pathway was more facile than that with EOR. [42] Thus, the slow rate of EOR kinetics can increase the amount of incompletely oxidized carbonaceous residues on the

GO/Co_3O_4 catalyst surfaces, which subsequently block the catalyst active sites and then inhibit the anodic reaction rate. [43] Furthermore, the increased number of carbon atoms of ethanol (CH_3CH_2OH) can gradually diminish the catalytic activity because of the C–C bond cleavage and the reaction intermediates, leading to the restriction of EOR kinetics.

To further assess the reproducibility of the mesoscopic porous hybrid GO/Co_3O_4 for AOR, the retention of long-term electrode efficiency was investigated through continuous cycling in 1 M methanol at a 50 mVs^{-1} scan rate (**Figure 6A**). The current oxidation density at 0.6 V performs 75.43% retention of its original value after 1000 cycles. This reduction of the electro-oxidation capacity (~24%) with successive potential scans might result from the consumption of ethanol and adsorption of oxidative intermediates, such as CO, CO_2, HCOOH, HCOH, and $HCOOCH_3$ at the electrode surfaces; this subsequently poisoned the electrode. [44–47] However, in the fresh electrolyte-based methanol oxidation assay, the current density at 0.6 V retained 85.2% of its original value after 1000 cycles. The retention of electrocatalytic activity might have resulted from the unique structural stability of GO/Co_3O_4/GC sheet racks.

(Figure 6)

Durability of the electrode catalyst is an evoked factor to evaluate the performance of DAFCs. Current-time relationships were measured using chronoamperometry technique in the presence of 1.0 M ethanol and methanol at an applied voltage of 0.55 V (*vs.* Hg/HgO) for 10,000 s (**Figures 6B–C and S11**). At the beginning of AOR, the oxidation currents of the GO/Co_3O_4/GC rack-, S-GO/Co_3O_4/GC block-, and Co_3O_4/GC rack-based electrodes were relatively high, indicating improved reaction kinetics at the applied potential. The Co_3O_4/GC racks-based electrode shows a sharp L-curve decay in the oxidation current at the initial time of AOR. In turn, the GO/Co_3O_4/GC rack- and S-GO/Co_3O_4/GC block-based electrodes show a pseudo-steady state of a gradual decay up to 10000 s (**Figure 5B–C**). Furthermore, the current density increased in the order GO/Co_3O_4/GC > S-GO/Co_3O_4/GC > Co_3O_4/GC during the whole elapsed time, indicating the superior electroactivity and fast reaction kinetics of the GO/Co_3O_4/GC rack-based electrode. The drop in the current density was attributed to the accumulation of alcohol molecules and intermediates on the electrode surfaces, leading to poisoned electrodes. Significantly, the current density at the end of the test duration (10000 s) of the GO/Co_3O_4/GC racks was higher than that of the S-GO/Co_3O_4/GC blocks, indicating the effect of hierarchal sheet racks in the enhancement of the poisoning resistance. The slight decay curve in the GO/Co_3O_4/GC-based electrode indicates the stability of vertical and non-stacked edge scale of the sheet racks with a running time of 10000 s.

To evaluate the charge transfer resistance and AOR kinetics of GO/Co_3O_4/GC rack-, S-GO/Co_3O_4/GC block-, and Co_3O_4/GC rack-based electrode catalysts, electrochemical impedance spectroscopy profile was employed on an open circuit potential with a 5 mV amplitude in the range of 100 kHz to 0.01 Hz in 0.5 M NaOH. The Nyquist plots (**Figure 6D**) of the catalysts show similar behavior, with a semicircle at high frequency and a straight line at low frequency corresponding to the related charge transfer resistance and capacitive behavior of Co_3O_4. [42] The equivalent circuit components of solution resistance (Rs), redox capacitance (C), and charge-transfer resistance (Rct) are due to electrolyte resistance, charge-transfer resistance, and redox capacitance, respectively. The semicircle diameters (Figure 6D, insert) decrease in the order GO/Co_3O_4/GC < S-GO/Co_3O_4/GC < Co_3O_4/GC, indicating that the GO/Co_3O_4/GC racks have the highest charge transfer and electronic configuration.

The electrochemical findings (Figures 4 and 6) clearly show the benefits obtained through our proposed catalyst and confirm its excellent activity for alcohol electrooxidation under alkaline conditions compared with that of commercially used Pt/C electrode. For example, the chronoamperometric response (Figure 6B–**6**C) indicated that the GO/Co_3O_4 catalyst was less poisoned by the adsorbed species and intermediates. Along with this result, the present catalyst showed excellent durability compared with the commercially available Pt/C (20 wt% Pt), as illustrated in **Figure S14**. Our findings, in general, showed evidence that the increased current density and lower onset potential are indicative of the excellent activity of GO/Co_3O_4 rack catalyst compared with the previous reports on noble metal catalysts in real DEFC. [48] Moreover, the durability test (**Figure 6)** under potential cycling conditions revealed that the GO/Co_3O_4 rack catalyst had superior stability than other noble-metal free electrocatalysts (Table S2 and related references), thereby indicating its potential feasibility in DAFC systems.

The superior electroactivity of the GO/Co_3O_4/GC electrode catalyst in terms of current oxidation density, low onset potential and charge transfer capacitance, long-term stability and reproducibility, surface electron movement, and molecular alcoholic diffusivity (Scheme 1) indicates that the proposed hybrid GO/Co_3O_4 racks might benefit from the integrative contribution of both the Co^{3+} component and the carbon support. Moreover, the vertically fattened GO/Co_3O_4 sheet racks with mesoscopic window-room entrances, marginal protruding ridge-like arms, and double-diffusive mesopores (i.e., 5.4 and 14.4 nm, Figure 3B) enable (i) fast electrical charge movements by maximizing the diffusion and density of trigger pulse electrons during AOR; (ii) offers more accessible sponge-like interfaces that may form between the electrolyte and GC-modified electrode; and (iii) hooks the ethanol/methanol

molecules. The mesospace-window hooks, dense and active {112}/{111} Co^{3+} and O^{2-} sites, long-range sheet ordering, vertical sheet racks, mimicked sharp-pointed outgrowth prickles covered with sheath surfaces, and non-stacked layers enable electron diffusion and movements with little resistance and ensure contact between every mesocrystal surfaces and the electrolyte in a multi-directional accessibility. Furthermore, the structural stability of GO/Co_3O_4/GC sheet with neat micro/nano-groove room, butterfly wing scale, and wall grove hierarchy greatly improves the electrical conductivity and electron transport. The GO/Co_3O_4 sheet racks with {112} plane and interface-generated surface {112}/{111} provide more catalytically active and chemically active sites, as well as facile electron movement along the surfaces of vertically oriented sheets and through the open pores that lead to fast reaction kinetics.

4. Conclusion

In summary, we developed a scalable and cost-effective one-pot route to synthesize mesoscopic porous S-GO/Co_3O_4 sheet-on-sheet blocks and GO/Co_3O_4 racks that are markedly oriented in (i) neat micro/nano-groove rooms, (ii) butterfly wing scales, and (iii) wall groves as efficient exposed surface anodic catalysts for DAFCs. Results showed that electron diffusion and movements with little resistance were attributed to the controlled mesospace-window hooks, dense and active {112}/{111} Co^{3+} and O^{2-} sites, long-range morphological sheet ordering, vertical sheet racks with mimicked sharp-pointed outgrowth prickles covered with sheath surfaces, and vertically non-stacked edge scales. These factors also ensure contact between the electrolyte and every active site located in a multi-directional accessibility, such as (i) surface domains, (ii) 3D central crystal, (iii) 1D dense plate sheet, and (iv) active-top-surface atom arrangement of Co_3O_4 MCs. Significantly, the GO/Co_3O_4 racks exhibit superior electroactivity for alcohol electrooxidation in terms of current oxidation density, low onset potential and charge transfer capacitance, long-term stability and reproducibility, surface electron movement, and molecular alcoholic diffusivity compared with those of S-GO/Co_3O_4 blocks and naked Co_3O_4. Importantly, the hybrid GO/Co_3O_4 catalyst shows improved long-term durability of up to 10000 s, which may have resulted from its excellent structural stability. This finding opens a new avenue for massive-scale fabrication of efficient electroactive catalysts and for the practical use of DAFCs.

5. Experimental section

5.1 Synthesis of mesoscopic hybrid sheet GO/Co_3O_4 racks and S-GO/Co_3O_4 blocks

The mesoscopic hybrid sheet-on-sheet GO/Co_3O_4 racks and S-GO/Co_3O_4 blocks were synthesized through one-pot and simple hydrothermal protocol. For the typical synthesis of S-GO/Co_3O_4 blocks, 0.1 M of $CoCl_2 \cdot 6H_2O$ (1.428 g) and 1.0 M of urea (3.6 g) was first dissolved in 60 mL Milli-Q water through stirring until a clear pink solution was obtained. Second, 80 mg of GO was fabricated from natural graphite powder (see Supporting Information), dispersed into the reaction solution, and subsequently stirred for 3 h to evenly disperse the GO. Third, the resulting slurry was sealed in a Teflon-lined stainless and thermally treated at 160 °C for 12 h before cooling naturally to room temperature. The obtained GO/$Co(CO_3)_{0.5}(OH)_x \cdot 0.11H_2O$ precipitate was filtered, rinsed with double distilled water followed by absolute ethanol several times, and then dried in air for 12 h at 80 °C. Fourth, the GO/$Co(CO_3)_{0.5}(OH)_x \cdot 0.11H_2O$ powder was heated to 400 °C with a ramp of 5 °C min^{-1} under argon flow and annealed at the peak temperature for 4 h to obtain S-GO/Co_3O_4 nanocomposite sheets. Following the typical procedure, the addition of 0.5 M HMTA (4.205 g) instead of urea in the first step led to the fabrication of sheet-on-sheet GO/Co_3O_4 racks. Furthermore, the Co_3O_4 sheet racks were fabricated without the addition of GO powder.

References

[1] A.S. Arico, P. Bruce, B. Scrosati, J.M. Tarascon, W. Van Schalkwijk, Nat. Mater. **2005**, 4, 366.

[2] X.M. Ren, P. Zelenay, S. Thomas, J. Davey, S. Gottesfeld, J. Power Sources **2000**, 86, 111.

[3] S.K. Kamarudin, W.R.W. Daud, S.L. Ho, U.A. Hasran, J. Power Sources **2007**, 163, 743.

[4] C. Liu, F. Li, L.P. Ma, H.M. Cheng, Adv. Mater. **2010,** 22, E28.

[5] Y. Lu, J.P. Tu, C.D. Gu, X.H. Xia, X.L. Wang, S.X. Mao, J. Mater. Chem. **2011**, 21, 4843.

[6] E. Antolini, J. Power Sources **2007**, 170, 1.

[7] Y. Lu, J.P. Tu, C.D. Gu, X.H. Xia, X.L. Wang, S.X. Mao, J. Mater. Chem. **2011,** 21, 4843.

[8] Y.S. Li, T.S. Zhao, Z.X. Liang, J. Power Sources **2009,** 190, 223.

[9] H.H. Wang, Z.H. Sun, Y. Yang, D.S. Su, Nanoscale **2013**, 5, 139.

[10] H.P. Liu, J.Q. Ye, C.W. Xu, S.P. Jiang, Y.X. Tong, J. Power Sources **2008,** 177, 67.

[11] H.J. Huang, X. Wang, J. Mater. Chem. **2012**, 22, 22533. Y. Qiu, L. Zhiyi, S. Xiaoming, L. Junfeng, Sci. Rep. **2013**, 3, 3537.

[12] a) S. K. Meher, G. R. Rao, J. Phys. Chem. C **2011**, 115, 15646. b) S.K. Meher, G.R. Rao, J. Phys. Chem. C **2013**, 117, 4888.

[13] a) M. Chen, B. Wu, J. Yang, N. Zheng, Adv. Mater. **2012,** 24, 862. b) K. D. Ashok, K. L. Rama, H. K. Nam, J. Daeseung, H. L. Joong, *Nanoscale* **2014,** 6, 10657.

[14] a) N. Spinner, W.E. Mustain, Electrochim. Acta **2011,** 56, 5656; b) W. Huanlei, M. Nan, S. Jing, W. Qigang, Y. Wenhua, W. Xin, *ACS Appl. Mater. Interfaces* **2015**, 7, 2882.

[15] a) J.B. Wu, Z.G. Li, X.H. Huang, Y. Lin, J. Power Sources **2013,** 224, 1. b) Q. C. Shuang, W. Yong, *J. Mater. Chem*. **2010,** 20, 9735.

[16] Y.C. Zhao, S.L. Nie, H.W. Wang, J.N. Tian, Z. Ning, X.X. Li, J. Power Sources **2012,** 218 320.

[17] J. Xiao, Q. Kuang, S. Yang, F. Xiao, S. Wang, L. Guo, Sci. Rep. **2013,** 3, 2300.

[18] F. Ji, H. C. Zeng, Chem. Mater. **2003,** 15, 2829.

[19] X.W. Xie, Y. Li, Z.Q. Liu, M. Haruta, W.J. Shen, Nature **2009,** 458, 746.

[20] H. Linhua, P. Qing, L Yadong, J Am Chem Soc. **2008,** 130, 16136.

[21] Y.Y. Liang, Y.G. Li, H.G. Wang, J.G. Zhou, J.J. Wang, T. Regier, H.J. Dai, Nat. Mater. **2011,** 10, 780.

[22] J.P. Alper, A. Gutes, C. Carraro, R. Maboudian, Nanoscale **2013,** 5, 4114.

[23] X.C. Dong, H. Xu, X.W. Wang, Y.X. Huang, M.B. Chan-Park, H. Zhang, L.H. Wang, W. Huang, P. Chen, ACS nano **2012,** 6, 3206.

[24] Z. Genqiang, W. L. Xiong, *Adv*. *Mater*. **2013,** 25, 976.

[25] P.D. Yang, D.Y. Zhao, D.I. Margolese, B.F. Chmelka, G.D. Stucky, *Nature*, **1998**, 396, 152.

[26] L.X. Sheng, S.C. Jun, W.L. Xiong, C.Z. Hua, Adv. Funct. Mater. **2012,** 22, 861.

[27] H. Nguyen, S.A. El-Safty. J. Phys. Chem. C **2011,** 115, 8466.

[28] Y. Zhao, S. Chen, B. Sun, D. Su, X. Huang, H. Liu, Y. Yan, K. Sun, G. Wang, Sci. Rep. **2015,** 5, 7629.

[29] J. Zhu, L. Huang, Y. Xiao, L. Shen, Q.i Chen, W. Shi, Nanoscale **2014,** 6, 6772.

[30] A.C. Ferrari, Phys. Rev. Lett. **2006,** 97, 1.

[31] D. Ye, L. Luo, Y. Ding, B. Liu, X. Liu, Analyst **2012,** 137, 2840.

[32] C. S. Park, K. S. Kim, Y. J. Park, J. Power Sources **2013,** 244, 72.

[33] S.W. Zhong, R. Wencai, W. Lei, G. Libo, Z. Jinping, C. Zongping, Z. Guangmin,, L. Feng, M. C. Hui, ACS Nano **2010**, 4, 3187.

[34] M. A. Prathap, R. Srivastava, Nano Energy **2013,** 2, 1046.

[35] M. Jafarian, M.G. Mahjani, H. Heli, F. Gobal, H. Khajehsharifi, M.H. Hamedi, Electrochim. Acta **2003,** 48, 3423.

[36] M. Fleischmann, K. Korinek, D. Pletcher, J. Electroanal. Chem. **1971,** 31, 39.

[37] I.G. Casella, M. Gatta, J. Electroanal. Chem. **2002**, 534, 31.

[38] M. Watanabe, S. Motoo, *J. Electroanal. Chem.* **1975**, 60, 275.

[39] A.J. Motheo, E.R. Gonzalez, G. Tremiliosi-Filho, P. Olivi, A.R. Andrade, B. Kokoh, J-M. Le´ger, E.M. Belgsir, C. Lamy, *J. Braz. Chem. Soc*. **2000**, 11, 16.

[40] L. Qian, L. Gu, L. Yang, H.Y. Yuan, D. Xiao, Nanoscale **2013**, 5, 7388.

[41] X.L. Tong, Y. Qin, X.Y. Guo, O. Moutanabbir, X.Y. Ao, E. Pippel, L.B. Zhang, M. Knez, Small, **2012,** 8, 3390.

[42] C. Lamy, E.M. Belgsir, J.M. Leger, *Journal of Applied Electrochemistry* **2001**, 31, 799.

[43] C. Xu, R. Zeng, P.K. Shen, Z. Wei, *Electrochimica Acta*. **2005**, 51, 1031.

[44] Z.B. Wang, G.P. Yin, J. Zhang, Y.C. Sun, P.F. Shi, J. Power Sources **2006,** 160, 37.

[45] S. García-Rodríguez, S. Rojas, M. Peña, J. Fierro, S. Baranton, J. Léger, Appl. Catal. B **2011,** 106, 520.

[46] M. Heinen, Z. Jusys, R., J. Behm, J. Phys. Chem. C **2010**, 114, 9850–9864.

[47] L. Jianping, Y. Jianqing, X. Changwei, P. J. San, T. Yexiang, Electrochem. Commun. **2007**, 9, 2334.

[48] W.J. Zhou, W.Z. Li, S.Q. Song, Z.H. Zhou, L.H. Jiang, G.Q. Sun, Q. Xin, K. Poulianitis, S. Kontou, P. Tsiakaras, *Journal of Power Sources* **2004**, 131, 217.

Figure 1

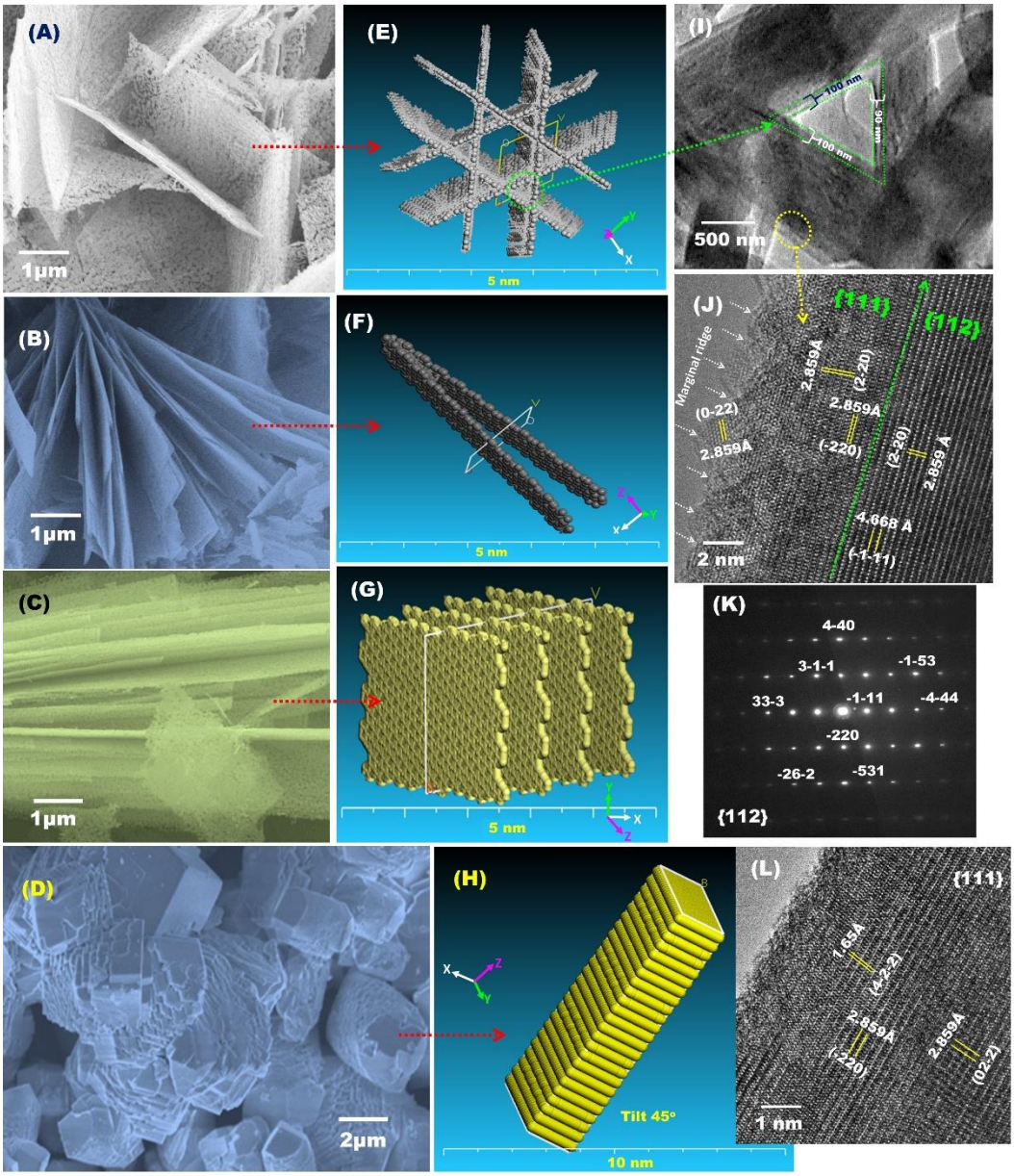

Figure 1. Top-view FE–SEM images of the hierarchical GO/Co_3O_4 sheet racks (A–C) and stacked sheet blocks (D) fabricated via a facile one-pot hydrothermal approach. The DFT molecular structure simulations of hierarchically GO/Co_3O_4 non-stacked sheet racks (E-G) showed three basic types of scalability in different orientational shapes such as a neat of micro/nano-groove rooms (E), butterfly wing scales (F), and wall groves (G), and stacked S-GO/Co_3O_4 sheet-on-sheet blocks oriented in vertical tower shapes (H). (I, J) low-and high magnification of HAADF-STEM micrographs of mesoscopic porous hybrid GO/Co_3O_4 at different locations illustrating the porous nature of the sheet racks shaped in a neat of groove rooms. (J) High magnification HAADF-STEM micrographs showing the atomic structure of the developed nanostructures along the dominant {111/112} plane of interfaces. (K) The corresponding electron diffraction (ED-STEM) pattern down the projection {112} plane. (L) High magnification HAADF-STEM micrographs showing the atomic structure of the developed stacked sheet blocks along the top dominant {111} plane.

Figure 2

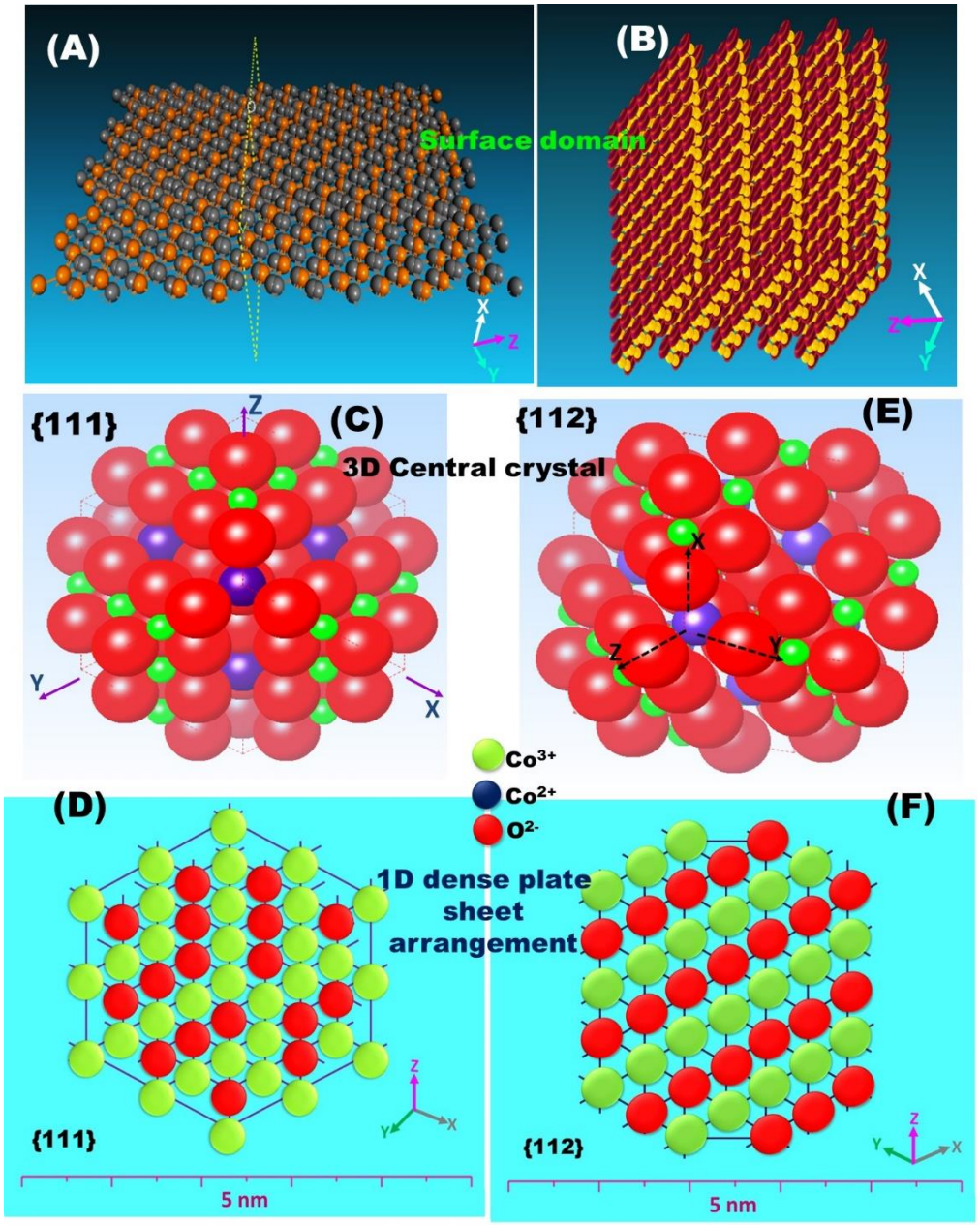

Figure 2. (A–F) Schematic representation of the surface domain modeling by DFT of hierarchically stacked S-GO/Co_3O_4 sheet-on-sheet blocks (A, C, and D) and GO/Co_3O_4 **non-stacked** sheet racks-like wall groves that vertically aligned (B, E and F). (C, E) Theoretical modeling by DFT of three-dimensional (3D) simulation models of the central S-GO/Co_3O_4 and GO/Co_3O_4 crystal projections along the {111} (C), and {112} (E) planes, respectively. (D, F) The central, dense arrangement of active Co^{3+} (green), and O^{2-} (red) sites along the 1D crystal center of S-GO/Co_3O_4 (D) and GO/Co_3O_4 (F) crystal projections along the {111} (D), and {112} (F) planes.

Figure 3

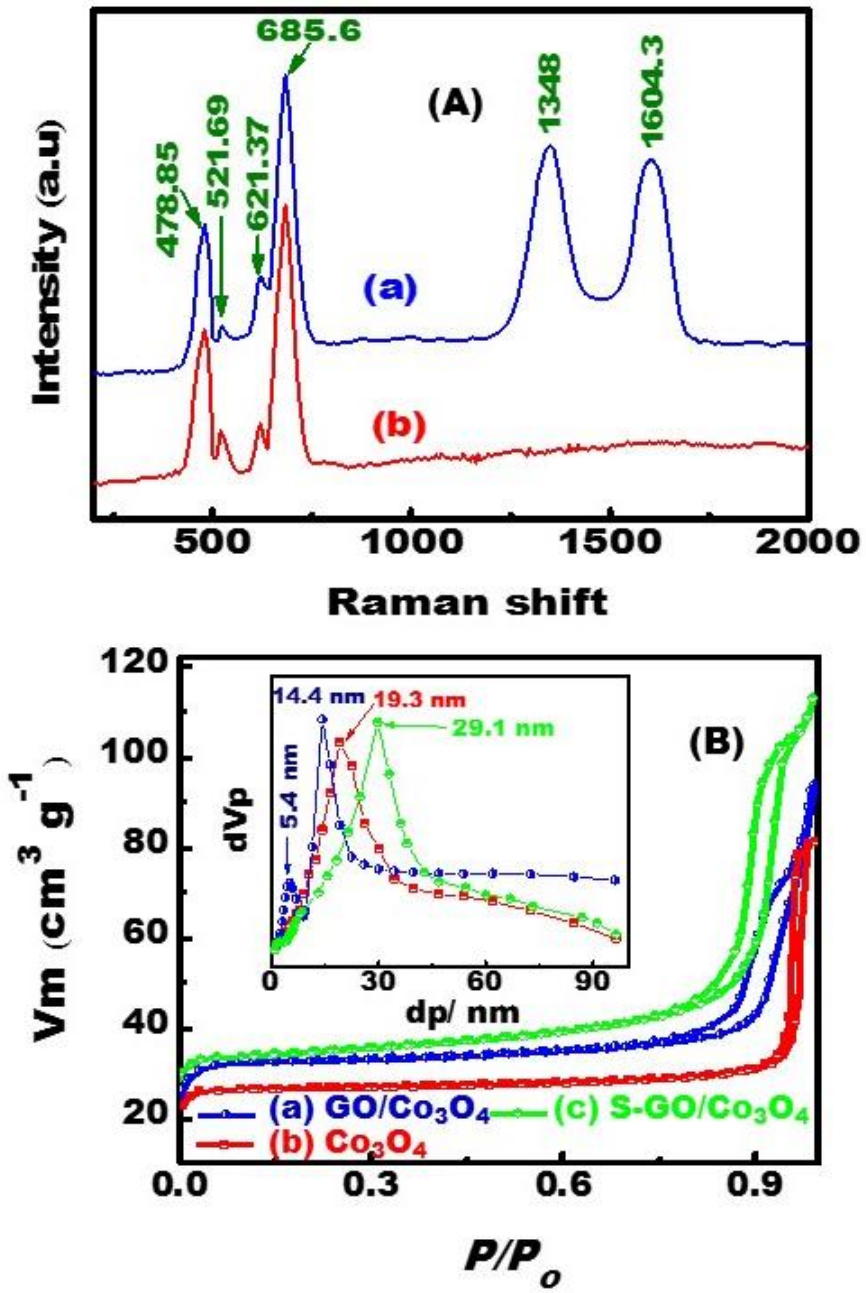

Figure 3 Raman spectroscopy investigations of the mesoscopic porous GO/Co_3O_4 (a) and Co_3O_4 (b) sheet racks. The Raman shift spectra of GO/Co_3O_4 (a) and Co_3O_4 (b) measured at a laser beam intensity of 633 nm. (B) N_2-adsorption/desorption patterns measured at 77K and the corresponding pore size distributions of the calcined GO/Co_3O_4 (a) and Co_3O_4 (b) sheet racks, and S- GO/Co_3O_4 sheet-on-sheet blocks (c). The insert displays the related pore sizes analyzed by NLDFT theory. The y-axis of N_2 isotherms of S- GO/Co_3O_4 shifted vertically by 10 time in magnitude.

Figure 4

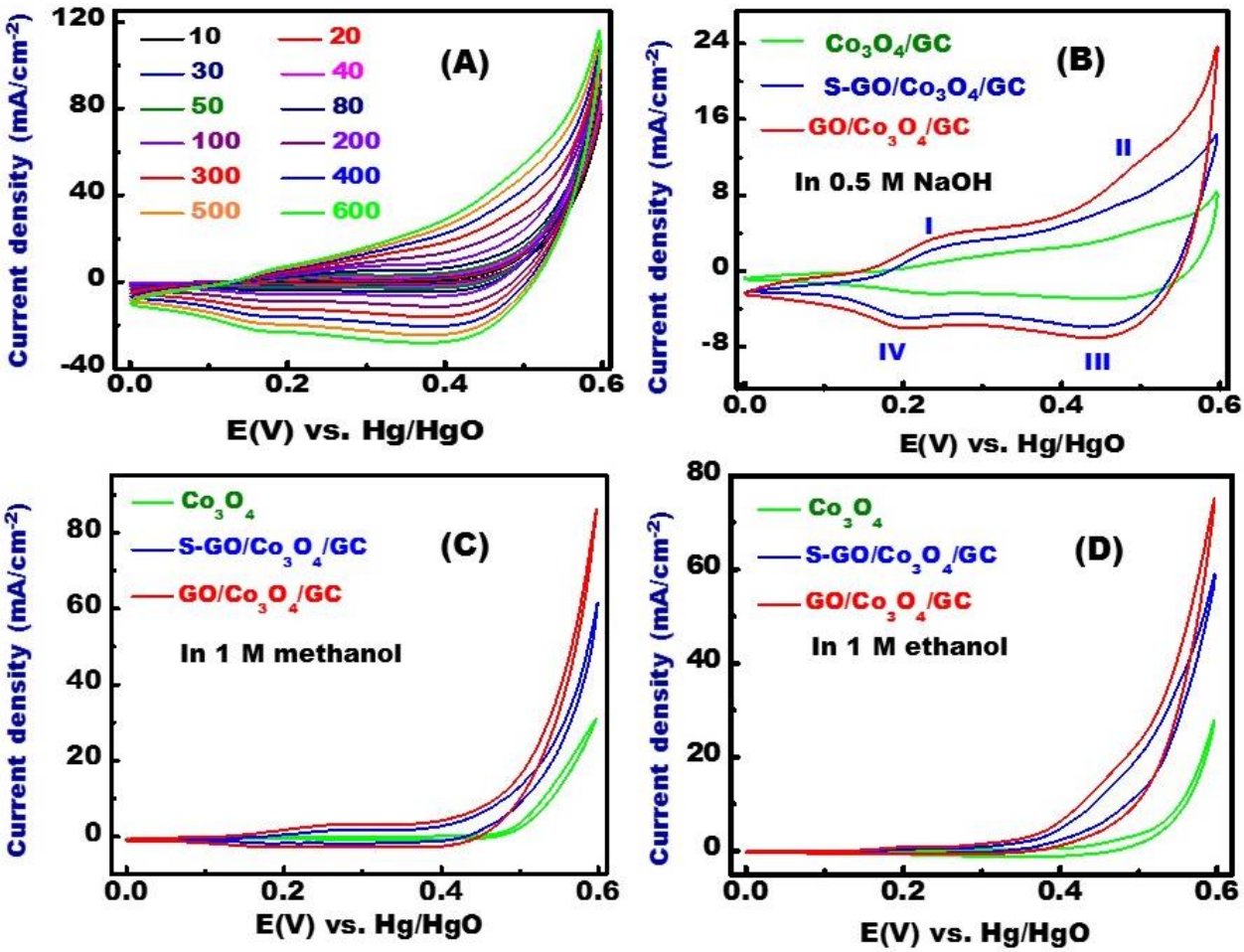

Figure 4 (A) CVs of mesoscopic porous hybrid GO/Co_3O_4/GC electrode racks recorded in 0.5 M NaOH N_2-saturated electrolyte in presence of 1 M methanol at room temperature and at various scan rates. (B–D) Electrochemical properties of Co_3O_4/GC, GO/Co_3O_4/GC, and S-GO/Co_3O_4/GC electrodes recorded in 0.5 M NaOH N_2-saturated electrolyte in the absence or presence of 1 M ethanol or methanol at a scan rate of 50 mV s^{-1} at room temperature. (B) CV profiles of the modified electrodes in 0.5 M NaOH, (C) CVs of the modified electrodes recoded in 1 M methanol, and (D) CVs of the modified electrodes recoded in 1 M ethanol.

Scheme 1

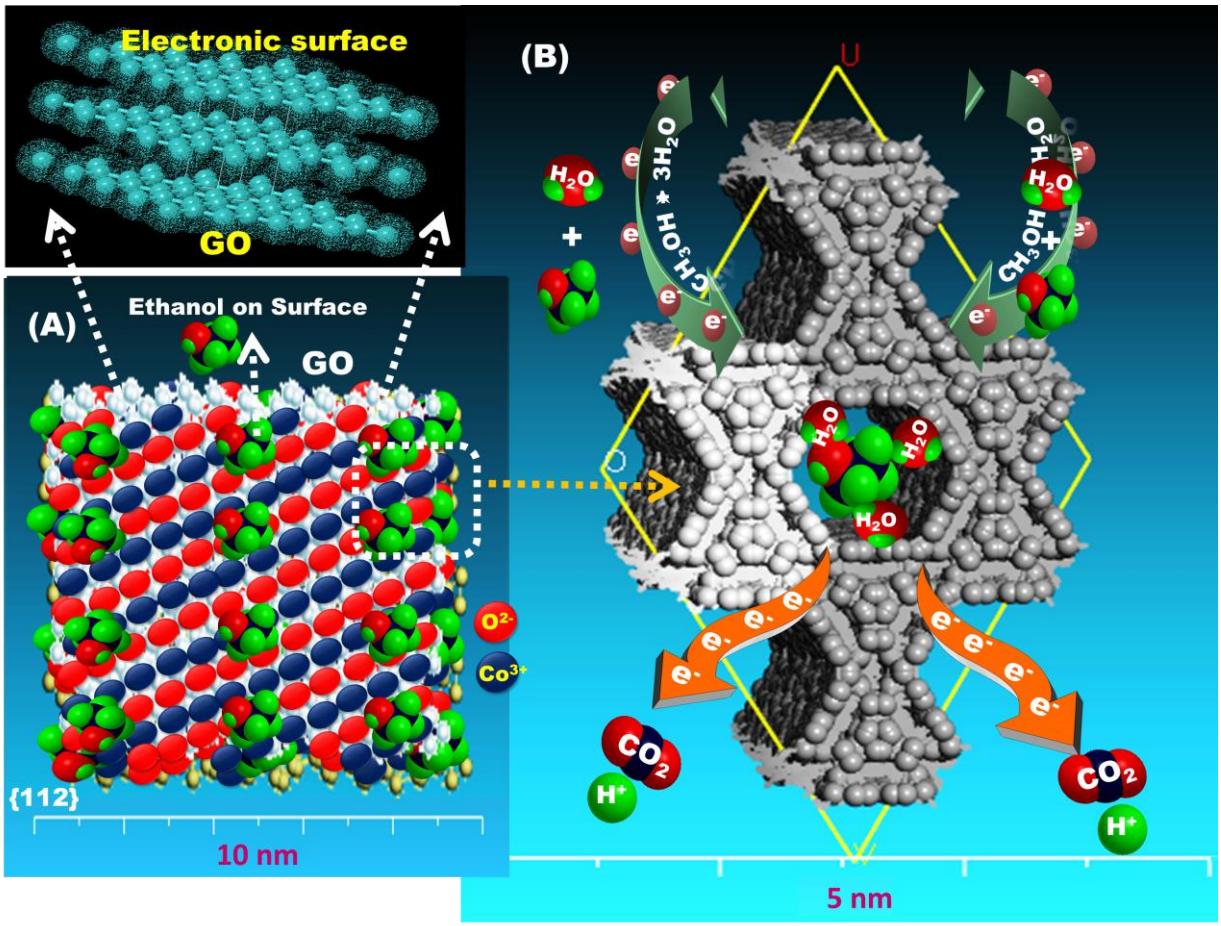

Scheme 1. Schematic mechanism of electrooxidation of ethanol or methanol in multiple steps, resulting in 12 or 6 electrons transferred from the electrolyte phase, respectively, to the binding active plane {112} sites measured by density functional theory (DFT). (A &B) the diffusion pathways of alcohol molecules (ethanol) along the interior-double layered GO/Co_3O_4 sheet surfaces (A) and along the crystal center (B) oriented into the mesospace voids of the hierarchical GO/Co_3O_4 sheet structures. (A-top) An orientational view of the GO dense electronic surface layers along the hierarchical GO/Co_3O_4 sheet racks. We strongly believe that the alcohols molecules react with CoOOH layer and produce CO_2. While the Co species and unoxidized intermediates accumulate at the catalyst surface and over active sites and subsequently poisoning the catalyst, leading to block the exposed active sites, reduce the oxidation current, and further weak the reaction kinetics.

Figure 5

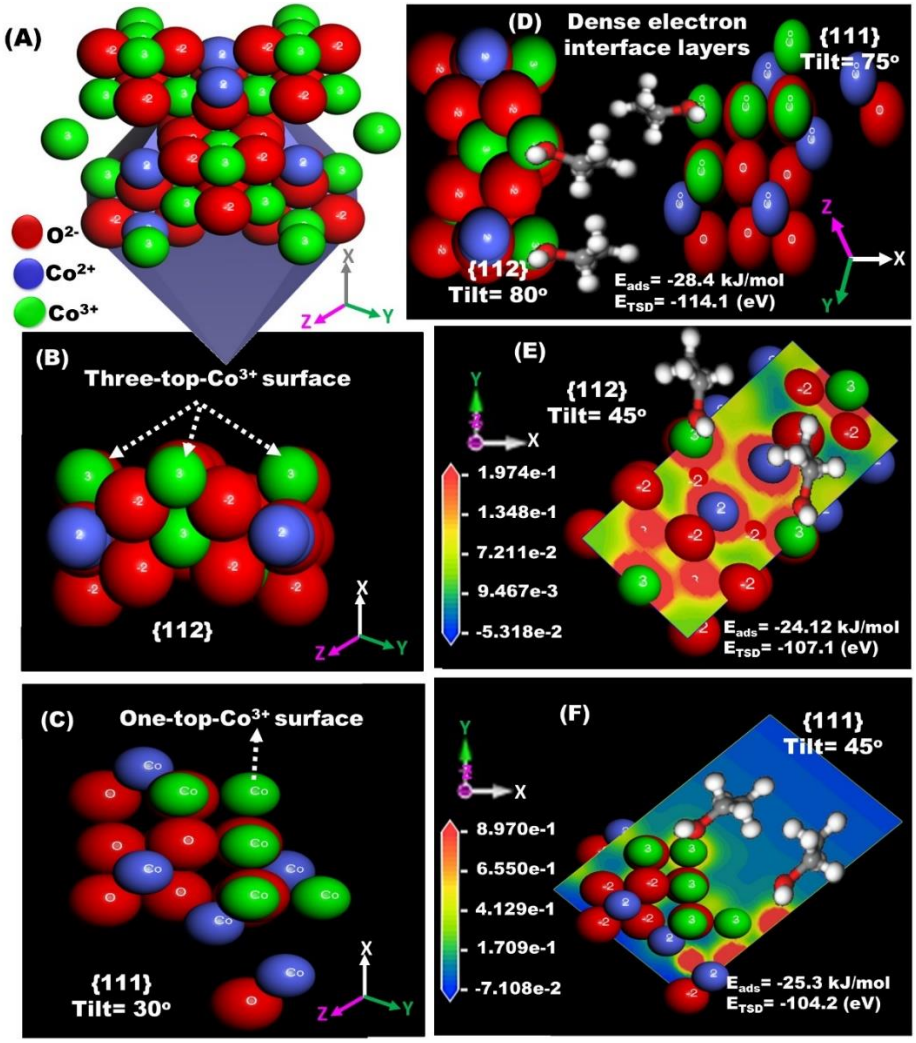

Figure 5 (A–D) DFT theoretical models of Co_3O_4 crystal structures of both sheet racks and blocks (A), top-surface crystal unit (B-D), and (E,F) the distribution of electrostatic potential (EP) and vertically geometric ethanol-to-surface orientation (E-F) at the catalytically active surfaces of GO/Co_3O_4 sheet racks along the single crystal {112} (B) and interface crystal {112}/{111} (D) planes, and the active surfaces of S-GO/Co_3O_4 sheet blocks along the single crystal {111} plane (D) that dominated in the hierarchal Co_3O_4 structures (A). (E-F) Optimized molecule-to-surface binding structure along the single crystal {112} (E), and {111} (F) planes of GO/Co_3O_4 sheet racks and S-GO/Co_3O_4 sheet blocks, respectively. The molecular orientation of ethanol molecule in vertical alignment around the potential electron distribution surfaces indicates the dense configuration around the active positively (Co^{3+}) and negatively (O^{2-}) charged atoms on the top-exposed surfaces of crystal {112}/{111} interface (D), and {112} (E) plane of GO/Co_3O_4 sheet racks, and {111} (F) plane of S-GO/Co_3O_4 sheet blocks, respectively. Insert (D-F) are the adsorption energy (Eads) and thermodynamically stable binding energy (E_{TSB}) of ethanol onto {111}/{112} (D) and{112} (E) of GO/Co_3O_4 sheet racks, and {111} (F) planes of S-GO/Co_3O_4 sheet blacks that calculated by DFT.

Figure 6

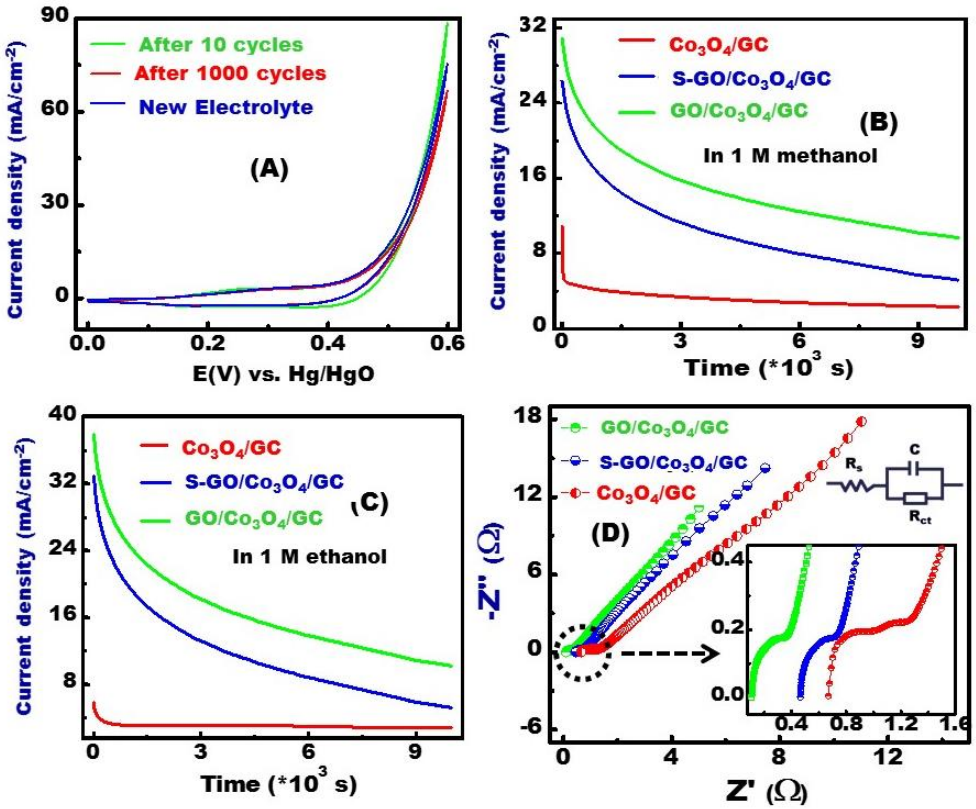

Figure 6 (A) CVs of mesoscopic porous hybrid GO/Co_3O_4/GC electrode recorded in 0.5 M NaOH N_2-saturated electrolyte in presence of 1 M methanol at room temperature after continuous cycling. (B, C) Long term stability recorded by CA test of Co_3O_4/GC and GO/Co_3O_4/GC electrode sheet racks, and S-GO/Co_3O_4/GC electrode sheet blocks recorded in 0.5 M NaOH N_2-saturated electrolyte and 1 M alcohols for 10,000 s at a fixed potential of 0.55 V (*vs*. Hg/HgO). (B) Current–time relationships in 1 M methanol, and (C) Current–time relationships in 1 M ethanol. (D) EIS profiles of Co_3O_4/GC and GO/Co_3O_4/GC electrode sheet racks, and S-GO/Co_3O_4/GC electrode sheet blocks recorded in 0.5 M NaOH solution and 1 M methanol at 5 mV amplitude. The equivalent circuit components described in the Nyquist plots are the redox capacitance (C), and solution resistance (Rs) of Co_3O_4/GC and GO/Co_3O_4/GC racks-, and S-GO/Co_3O_4/GC blocks-based electrodes and charge-transfer resistance (Rct) at the electrode–electrolyte interface, respectively.